Local flowfield about large distributed roughness in the initial ice accretion process

J. F. Winkler
Illinois Univ., Urbana

M. B. Bragg
Illinois Univ., Urbana

AIAA 34th Aerospace Sciences Meeting and Exhibit, Reno, NV Jan 15-18, 1996

An experimental investigation of the local flowfield about large isolated and distributed roughness placed in a flat-plate laminar boundary layer has been performed. Large roughness in this sense refers to roughness with a height to boundary-layer thickness, $k/delta$, greater than unity. This type of roughness typically occurs during the initial accretion of ice on an aircraft in flight. The roughness elements were hemispherical in shape, and the test conditions were run with a nominal roughness Reynolds number of 3900 and with $k/delta$ varying from 2.6 to 3.5. Fluorescent oil surface flow visualization was used in conjunction with 2D laser-Doppler velocimeter data to examine the flowfield over the clean plate, the isolated roughness, and the distributed roughness. Results showed at least three identifiable primary vortices in the horseshoe vortex system upstream of the isolated roughness and at least two primary vortices upstream of the distributed roughness. It was shown that the recirculation region behind the isolated roughness was larger and stronger than the recirculation region behind the distributed roughness. Comparison of velocity profiles downstream of the roughness indicated that the distributed roughness flowfield was further developed in the transition process than the isolated roughness flow field at any given location. (Author)

Local Flowfield About Large Distributed Roughness in the Initial Ice Accretion Process

J. F. Winkler[†] and M. B. Bragg[*]
University of Illinois at Urbana-Champaign

ABSTRACT

An experimental investigation of the local flowfield about large isolated and distributed roughness placed in a flat-plate laminar boundary layer has been performed. Large roughness in this sense refers to roughness with a height to boundary-layer thickness greater than unity, $k/\delta > 1$. This type of roughness is typical of the type of roughness that occurs during the initial accretion of ice on an aircraft in flight. The roughness elements were hemispherical in shape, and the test conditions were run with a nominal roughness Reynolds number (Re_k) of 3900 and with k/δ varying from 2.6 to 3.5. Fluorescent oil surface flow visualization was used in conjunction with 2D laser-Doppler velocimeter (LDV) data to examine the flowfield over the clean plate, the isolated roughness, and the distributed roughness. Results showed at least 3 identifiable primary vortices in the horseshoe vortex system upstream of the isolated roughness and at least 2 primary vortices upstream of the distributed roughness. It was shown that the recirculation region behind the isolated roughness was larger and stronger than the recirculation region behind the distributed roughness. Comparison of velocity profiles downstream of the roughness indicated that the distributed roughness flowfield was further developed in the transition process than the isolated roughness flowfield at any given location.

INTRODUCTION

The recent American Eagle ATR crash near Chicago is a tragic reminder of the consequences of allowing too much ice to accrete on an aircraft's wing or control surfaces during flight. While it is well understood that, under certain weather conditions, ice may accrete on surfaces exposed to the flow and degrade the performance of an aircraft, the ability to predict the shape of the ice accretion is still in a premature stage.

The ice accretion process is a complex problem composed of a two-phase flowfield, where a phase change is present when the water droplets freeze, and where the surface of the wing is constantly changing shape as the ice accretes on it. As a result, the NASA Lewis code commonly used to predict ice shapes, LEWICE, is constantly being improved in an attempt to provide the users with more accurate results.

Icing Review

Ice may accrete on an aircraft's surfaces when it flies into a cloud made up of super-cooled water droplets[1]. Depending on the ambient and aircraft surface conditions, the droplets will either impact the surface and immediately freeze; or impact the aircraft and partially freeze, thus forming a water-ice mixture; or impact the surface and not freeze at all. If the temperature of the ambient air is substantially below freezing and the liquid water content (LWC) of the cloud is low, the droplets will be more likely to immediately freeze completely on impact; these conditions promote the growth of what is typically called rime ice. Rime ice shapes on a wing typically conform to the shape of the leading edge and therefore present a minimal effect on performance. If the ambient air temperature is near freezing and the LWC of the cloud is high, the droplets are more likely to hit the surface of the aircraft and form a water-ice mixture due to incomplete freezing, and the resulting ice shapes are called glaze ice. Glaze ice shapes have been known to form horns that grow out into the incoming flow. These shapes may produce large regions of separated flow which severely affect the aircraft's performance.

Clearly, the local convective heat transfer over the airfoil plays a major role in the amount of ice accumulation in any particular region. A region with higher convective heat transfer, i.e. a larger amount of cooling, will experience a larger growth rate of ice accretion. The status of local boundary-layer flow will, in turn, affect the local heat transfer. A turbulent

---

[†]Graduate Research Fellow, Dept. of Aeronautical and Astronautical Engineering, member AIAA
[*]Professor, Dept. of Aeronautical and Astronautical Engineering, Associate Fellow AIAA

boundary layer will tend to have a much larger rate of heat transfer than a corresponding laminar boundary layer. Potapczuk and Reinmann[1] emphasize that

> *The convective heat flux is influenced by the development of the boundary layer on the rough iced airfoil surface. As such, the pressure distribution, roughness level, and transition process all play an important role in the ice growth process.*

It has been hypothesized by Hansman, et. al.[2,3] that the smooth-rough boundary that occurs in the developing ice accretions is the location of boundary-layer transition. In other words, it was assumed that the roughness initiated a trip to turbulent flow at its boundary. Kerho[4], however, found that "no fully developed turbulent boundary layers were observed to occur at the roughness location, even though roughness heights were substantially greater than empirically determined critical roughness heights required to cause transition." The roughness elements do trigger the beginning of the transition process, and therefore their effects are extremely important on the development of the local boundary layer and heat transfer. Kerho suggests that the "glaze ice accretion process is governed by very local effects on the scale of the individual (roughness) elements." Results from the leading-edge ice accretion study performed by Shin[5] on a NACA 0012 airfoil combined with the data of Kerho[4] confirmed that the roughness in the initial accretion has heights much larger than the local boundary layer thickness.

Roughness Review - Isolated 3D

The first investigation of the qualitative 3D flowfield about an isolated 3D element was performed by Gregory and Walker[6]. This particular study concentrated on the effect of isolated roughness elements on the transition process. Experimental data describing the critical heights of roughness for turbulent wedge formation were taken for a flat plate and two airfoils. The critical height was defined as the height of an element which would just give rise to the formation of turbulent wedges.

The experimental investigation centered around cylindrical elements with heights less than the local boundary-layer thickness. Flow visualization techniques were used to obtain as much information about the element flowfield structure as possible. In front of the cylinder, it was noted that as the flow approached the element, it encountered an adverse pressure gradient due to the presence of the element and thus separated off the surface. The fluid would then roll up into "horseshoe-shaped" vortices which would wrap around the sides of the cylinder and extend downstream in the longitudinal direction. As many as three horseshoe vortices were

observed, and the number appeared to depend of freestream velocity. The flowfield behind the element was found to be a function of the Reynolds number based on element height, Re_k. At low Re_k, the flow would follow the sides of the cylinder until it separated and rolled up into a pair of spiral vortices (one on each side) behind the cylinder. These spiral vortices would rise normal to the plate surface (parallel to the cylinder) until they reached the top of the cylinder, where they would be turned 90 degrees downstream by the freestream. As Re_k was increased to some critical value, a spreading wedge with its own fine structure would appear downstream of the cylinder, and the spiral vortices stayed intact. As Re_k was increased further, the horseshoe vortex system described above would form around the front of the cylinder. The flowfield at this point can be seen in Fig. 1, taken from Gregory and Walker[6]. If Re_k is increased any further, the "twin vortex filaments leaving the top of the cylinder break down, and eddies are shed." At this point, it was noted that the horseshoe vortex was "the most prominent feature of the flow."

Norman[7] investigated the mechanism by which the base flow that forms around a single 3D rectangular gate roughness element is perturbed to cause transition from laminar to turbulent flow. This study described the formation of three separate vortex systems about the element: (1) Horseshoe vortex system; (2) Spiral vortex trailing system; and (3) Vortex system produced by instability in the top shear layer. The experiment was performed using hot-wire anemometry and smoke flow visualization.

The horseshoe vortex system is formed when the oncoming flow separates from the surface of the plate due to the presence of the element and rolls up into vortices. While Gregory and Walker[6] saw as many as three primary vortices, Norman[7] saw an additional two vortices on a fence with a $k/\delta = 1.8$. Three of these vortices were primary vortices rotating in the same direction, and the remaining two vortices were secondary vortices rotating in a direction opposite to the primary vortices. The number of vortices appears to be a function of k/δ and element shape. This flowfield was quite complex, and therefore two separate physical models were created: (1) the Jet Maze model; (2) the Stairstep model. For the case being studied, it was discovered that the flow visualization supported the Jet Maze model, which can be seen in Fig. 2. As Re_k is increased, the laminar wake behind the element will see the formation of a turbulent wedge downstream, and as Re_k is increased further, the horseshoe vortex structure upstream of the element begins to oscillate and then become turbulent. It is noted that the vortex systems for other element shapes are similar.

The spiral system is formed when the flow around the sides separates from the surface, is drawn in behind

2

the element due to the low-pressure region there, and curls up into spiral vortices with axes which are perpendicular to the plate surface. As described above, when these vortices reach the top of the element, they are turned downstream by the high-speed flow. Norman states that for $k/\delta < 1$, the shear layers on the sides contribute to the formation of the spiral vortices and to the support structure of the top shear layer. When k/δ becomes larger than 1, these side shear layers will eventually contribute to the formation of a Von Karman vortex street.

The top shear system is formed from separation of the flow off the top surface of the element. For the rectangular fence tested in this study, there was a well-defined separation. For a sphere, however, the top shear layer is less defined since the location of the separation line depends on the flowfield properties upstream of the element. If the Reynolds number is low enough and there are no strong instabilities, the top shear layer will be stable. As the Reynolds number is increased, however, the shear layer will become unstable and eventually start shedding periodic vortices.

Acarlar and Smith[8] performed a thorough analysis of the role that hairpin vortices have in the transition process. The experimental study consisted of detailed flow visualization and hot-wire data of the shedding characteristics of a hemispherical roughness element. The authors looked at the role the hairpin vortex plays in the transition process and noted that there is a distinct similarity between the structure of the flow due to the hairpin vortices and that found in turbulent boundary layers.

Roughness Review - Distributed 3D

While the previous authors were interested primarily in the study of the flowfields about single roughness elements, there has also been interest in exploring the effects of distributed roughness on the flowfield and its transition to turbulence.

Kendal[9] performed an experiment to investigate the distortion of a flat-plate laminar boundary layer by single and distributed surface roughness and the corresponding effect on stability. The roughness height was small compared to the boundary-layer thickness. Velocity profiles were taken for the #80 grit distributed roughness. It was found that the velocity deficit profile of the distributed roughness reached out to the edge of the layer in contrast to the case of the single roughness element, where the deficit profile stayed in the lower 1/6th of the layer. Kendal theorized that the larger region of retarded flow was due to the displacement of low-momentum flow by the roughness and not due to retardation by viscosity effects. It was also noted that the distributed roughness in effect displaced the Blasius profile upward without changing its shape; this displacement was assumed to occur due to the volumetric displacement of the roughness itself and the retarded flow near the wall.

Corke, et. al.[10] investigated the effect on the transition process of distributed roughness with a nominal height one-half the boundary-layer displacement thickness. The experimental data were gathered using hot-wire anemometry and smoke flow visualization techniques. Corke found that if the value of $k/\delta^* > 1$ the distributed roughness causes the onset of early transition of the flow through a mechanism other than Tollmien-Schlicting enhancement. It was discovered, however, that smaller scale distributed roughness ($k/\delta^* = 0.5$) actually leads to early transition through Tollmien-Schlicting enhancement

The previous experiments involved flow visualization and velocity profiles taken behind and on top of the roughness since there was no easy way to measure flowfield quantities within the distributed roughness. Tadjfar, et. al.[11] devised a unique way of measuring the flow velocity around the elements within the distributed roughness. A flat plate and spherical roughness elements were constructed out of glass, and a fluid mixture of 58% mineral seal oil and 42% Sohio MDI 57 was used as the working fluid since its index of refraction matched that of the glass. Since the fluid, roughness elements, and the plate had the same index of refraction, a 2D laser-Doppler velocimeter (LDV) system could be used to measure the flow velocity within the distributed roughness. The roughness used in this study was submerged within the boundary layer. Mean velocity profiles were taken at three different values of the roughness Reynolds number, Re_k: (1) $Re_k = 160$, (2) $Re_k = 315$, and (3) $Re_k > 315$. The boundary-layer profiles were divided into an inner region from the wall to 1 to 1.5 roughness heights and an outer region from 1 to 1.5 roughness heights to the edge of the boundary layer. It was interesting to note that at each particular Re_k the boundary layer for the clean case and that part of the profile in the outer region of the rough case were essentially identical. In other words, the roughness displaces the profile upwards. Unlike Corke, et. al.[10], no Tollmien-Schlicting instabilities were discovered in the flowfield, but this may be due to a difference in the value of k/δ for the two experiments.

Roughness Review Summary

The majority of the reviewed roughness research dealt with roughness with heights less than the boundary-layer thickness, i.e. $k/\delta < 1$. The roughness found in the initial ice accretion process, however, has been shown[5] to have heights much greater than the boundary layer thickness, i.e. $k/\delta \gg 1$. The current study was thus undertaken to investigate the local flowfield about such large roughness.

3

EXPERIMENTAL PROCEDURE

The following description briefly illustrates the experimental apparatus and procedures used in this investigation.

Wind Tunnel

The wind tunnel used in this experiment is the low-speed 3'×4' test-section tunnel at the University of Illinois Subsonic Aerodynamics Laboratory. The tunnel is of open-return type with a 7.5:1 contraction ratio and is capable of reaching speeds of up to 160 mph in the test section. It has a four-inch thick section of honeycomb followed by four screens to maintain a low turbulence level within the test section. Tunnel speed is adjusted using an Eaton model AF5000 variable frequency drive.

Model

A large flat plate was chosen as the model for this study to make the measurement and flow visualization around the roughness elements as convenient as possible. The flat plate measures 4 ft across by 8 ft long and is installed horizontally 10 inches off the floor of the test section. The plate is constructed of 3/8 inch thick aluminum which was factory precision ground to a tolerance of ± 0.005" with a 25 rms finish. A half-round was machined into a short side of the plate to act as the leading edge of the plate, and the plate was polished to further improve the surface quality. The plate was pressure tapped along a line offset from each long side by 12 degrees starting from each leading-edge corner. The taps were used to insure that the plate has a zero pressure gradient, or at the least, a favorable pressure gradient such that a laminar boundary layer may exist over the entire plate.

A flap constructed of sheet metal and reinforced with a small aluminum angle is placed at the trailing edge of the plate in order to control the pressure gradient on the plate. Without the flap, there was an adverse pressure gradient present on the top of the plate, and a leading-edge separation bubble formed and reattached as a turbulent boundary layer a short distance downstream. Flow visualization was used to determine the flap angle required to remove the leading-edge bubble and allow the presence of laminar flow.

LDV System

A two-component, 4-watt, Ion-Argon laser-Doppler velocimetry (LDV) system was used to measure the velocity profiles before and after the roughness elements on the flat plate. The LDV system was capable of obtaining two velocity components simultaneously in a non-intrusive manner. This method was ideal for unsteady and/or separated flows where the presence of a measuring probe in the flowfield may alter the flowfield. Through the use of frequency shifting, the LDV system

was able to measure reverse flow. Khodadoust[12] provides an excellent description of the details of the UIUC LDV system.

The system is composed of an Innova model 70 4-watt Ion-Argon laser and a TSI fiber-optic system. The fiber-optic setup allows the laser and the sensitive optics to be kept in a clean, controlled environment while the sealed fiber probe at the other end of the fiber-optic cable may be placed in the harsher tunnel room environment. The fiber probe focuses the laser energy into the measurement volume and also receives the scattered light from the measurement volume; the scattered light is received from backscatter. A computer-controlled 3-D Velmex traverse system was used to position the fiber probe to its desired location.

The flow was seeded with olive oil particles using two TSI model 9306 atomizers. These atomizers produce olive oil particles with a mean particle diameter of less than 0.6 microns and a concentration of 4.0×10^6 particles/cc[13]. The olive oil particles are injected into the tunnel room upstream of the tunnel entrance. A household fan is then used to disperse the particles into the air before they reach the honeycomb.

Flow Visualization Techniques

In order to help to qualitatively explain the flowfield around the roughness elements, surface fluorescent-oil flow visualization and flowfield smoke-wire flow visualization techniques were performed.

The fluorescent-oil technique involved applying and then wiping off a base coat of synthetic motor oil to the surface of the plate around the elements. A mixture of mineral oil and fluorescent dye was then air-brushed onto the surface of the plate. The tunnel was then set to the desired speed. Fluorescent black light tubes and UV spot lights were used as light sources. Under the UV light, the oil would fluoresce and the surface streaklines would become apparent. Photographs were then taken using both standard 35mm film cameras and a Kodak DCS 200.

The smoke wire technique was set up using 0.007" DIA steel wire stretched between two magnetic supports. The magnetic supports were fastened to opposite walls of the tunnel. The 35 lbf rating on the supports was strong enough to keep adequate tension in the wire while still allowing easy adjustment of the location of the wire. Model train smoke fluid was applied to the wire using a Q-tip applicator. A simple DC power supply was used to heat the wire. A laser sheet was used to illuminate the smoke. A Sony Hi8 camcorder was used to take video, and still photographs were taken with 35mm cameras.

Simulated Roughness

The roughness elements were sized and spaced based on information obtained by Shin[5] in a leading-edge ice accretion study on a NACA 0012 airfoil in the

4

NASA Lewis Icing Research Tunnel. Results from Shin's study and the data of Kerho[4] show that roughness in the initial ice accretion may be characterized by the data shown in Table 1.

Table 1. Typical Roughness Parameters for Initial Glaze Ice Accretions.

Re_c	k/δ	Re_k
2.76×10^6	2.7 - 4.8	1497 - 3328
3.68×10^6	3.1 - 5.5	1996 - 4437
4.60×10^6	3.5 - 6.1	2495 - 5547

The idealized roughness shape and pattern is the same as that used by Kerho[4]. The individual elements are hemispheres constructed from phenolic ball knobs. The distributed roughness is spaced such that the centers of the individual elements are nominally 1.3 diameters apart, and the distributed pattern is shown in Fig. 3. In order to obtain the best combination of a high k/δ value and a low Re_k value to match the values given in Table 1, it is desired to locate the roughness as close to the leading edge as possible and keep the velocity of the freestream flow as low as possible. The important factors in determining the optimum roughness size and location were the flow quality in the tunnel at low speeds; the desire to place the element such that it does not disturb the flow at the leading edge of the plate; and the desire to test physically large elements for improved LDV flowfield resolution and flow visualization.

The diameter of the hemispherical roughness elements was 1.5 inches. The extent of the distributed roughness was limited to five rows in the flow direction. A test was performed in order to determine the closest proximity of the roughness to the leading edge and the lowest speed attainable. For the distributed case, the first row of the roughness was placed such that the centers of the elements were 9.0 inches (12 roughness heights) from the plate leading edge. The distributed roughness thus extended from $x = 9.0$ inches (12 roughness heights) from the plate leading edge to $x = 15.755$ inches (21 roughness heights) from the plate leading edge. The isolated element was centered at the same x location as the last row of the distributed roughness, $x = 15.755$ inches (21 roughness heights) from the plate leading edge. The tunnel freestream speed was set at 10 ft/s after an investigation showed adequate flow quality at that speed. The above roughness location and tunnel freestream velocity correspond to a nominal $k/\delta = 3.5$ and a $Re_k = 3900$ at the leading edge of the roughness and a $k/\delta = 2.6$ and a $Re_k = 3900$ at the trailing edge of the roughness for an ambient temperature of 68°F. A sketch of the flat plate showing the distributed roughness placement and the coordinate system directions is shown in Fig. 4.

Data Reduction and Error Analysis

Tunnel Speed

An IBM PC compatible 486 based data-acquisition system was used to measure the required test conditions. The freestream velocity is calculated from the measured pressure differential between the test section and inlet, the ambient temperature, and the ambient pressure. The uncertainty[14] in the measured freestream velocity of the tunnel is ±0.18 ft/s at a freestream velocity of 10 ft/s, an ambient temperature of 68°F, and an ambient pressure of 1 atm.

LDV Uncertainty

The error analysis for the LDV system used in this study was carefully analyzed by Khodadoust[12]. Briefly, the total effective systematic error due to the electronics and the optics varies from 0.65% to 0.85% of the measured particle velocity. The low data rate obtained from the backscatter set-up limited the number of samples that were taken due to time constraints. Data were taken in the random mode, and 1000 samples were taken for each velocity component at each spatial location. For a 30% turbulence intensity level and a 95% level of confidence, this corresponds to a statistical uncertainty in the mean velocity of about 2%. Likewise, for 1000 samples and a 95% level of confidence, there is a statistical uncertainty in the standard deviation of about 4.5%.

RESULTS AND DISCUSSION

Laminar Flow Validation

The flap angle was adjusted to maintain laminar flow on the plate. Once this angle was set, the pressure gradient on the plate was measured using the static pressure taps and a differential pressure transducer. The gradient was nearly zero, if not slightly favorable. The LDV was then used to measure the boundary-layer profiles on the surface of the plate. Figure 5 shows the variation in the normalized velocity u/U_{edge} in the x direction with the surface normal coordinate z/k. This profile was taken 23 roughness heights downstream from the leading edge of the plate. The solid circles represent the clean LDV data, and the solid line represents the theoretical Blasius profile. There is excellent agreement between theory and experiment, and this shows that the flow over the clean plate is laminar.

Fluorescent-Oil Flow Visualization

Figure 6 is a photograph of the surface-oil flow around the isolated roughness element. Flow direction is from left to right, and the tick marks on the plate centerline are located 2 and 6 roughness heights downstream from the center of the element, respectively. Dark areas in the photograph indicate regions of high

5

shear where the oil has been scrubbed off, while lighter areas represent regions of lower shear where the oil still remains. Note that there are at least three distinct dark bands in front of the element which wrap around the element and trail downstream. Closer inspection of the original photograph reveals what appears to be an additional 2 bands, but they are substantially lighter. All of these bands represent the location of the aforementioned horseshoe vortices[6,7]. Again, these vortices are formed when the oncoming flow separates from the surface of the plate and the boundary-layer vorticity rolls up into one or more primary vortices. These vortices then wrap around the hemisphere and trail downstream.

The two bright lobes centered about the rear of the hemisphere in Fig. 6 indicate the presence of a spiral vortex system. Both the horseshoe vortex system and the spiral vortex system are quite similar to those diagrammed by Gregory and Walker[6] in Fig. 1.

Figure 7 is a photograph showing the oil flow at the leading edge of the distributed roughness. The bright element is on the centerline of the plate, and the flow direction is from bottom to top. There are two distinct dark bands which wrap around the front of each element and end in a bright spot in the space between the elements. Again, these dark bands represent the presence of a horseshoe vortex system in front of each element. Also note that there are dark bands that run parallel to the plate centerline and lead up to their respective bright spot in the space between the elements. These parallel bands likely indicate that the flow is accelerating toward the space between the elements, and that in this accelerated region, there is higher shear. The bright spots represent areas where fluorescent oil has pooled. Care should be taken when trying to interpret the surface flowfield past these pools since it was difficult to properly apply and then wipe off the synthetic oil basecoat that is required for adequate surface flow of the mineral oil topcoat. Therefore no observations will be made for this region.

Laser-Doppler Velocimeter Data

All quantitative data discussed in the following sections was taken in the xz plane along the centerline of the plate ($y/k = 0$). Again, recall from Fig. 4 that the x-direction is positive in the streamwise direction of the flow and that the z-direction is normal to the surface of the plate and positive upwards.

Global Flowfield

Figures 8, 9, 10, and 11 show the global flowfield variation in the mean velocity u/U_∞ in the x-direction, the mean velocity w/U_∞ in the z-direction, the turbulence intensity u'_{rms} of the x-component of velocity, and the turbulence intensity w'_{rms} of the z-component of velocity, respectively, in shaded contour plots.

Figure 8 shows the global flowfield variation of the mean velocity u/U_∞ for the clean, isolated roughness, and distributed roughness cases. The clean plot shows the gradual increase in the height of the boundary layer as the distance x increases down the plate that is typical of a flat-plate laminar boundary layer. This trend is duplicated in the isolated roughness plot up to about an $x/k=16$, which is 4 roughness heights ($4k$) upstream of the leading edge of the hemisphere. At this point, there is a noticeable thickening and retardation of the flow due to the adverse pressure gradient caused by the presence of the isolated element. In the region 2 roughness heights upstream of the element, a reverse flow region exists near the plate surface. This region indicates the presence of the horseshoe vortex system discussed earlier in the oil flow visualization. Downstream of the isolated roughness, there is a separation pocket denoted by another reverse-flow region that extends about 2 roughness heights downstream of the back of the hemisphere to an x/k of about 24, where the flow reattaches to surface of the plate. As the distance x/k is further increased, a large retarded flow region typical of a developing wake behind a body is apparent.

In the distributed roughness plot, there is a slight global retardation of flow upstream of the roughness to accompany the local retardation immediately upstream of the first row of elements. Again, note that there is a reverse-flow region near the surface of the plate that starts about 1.5 roughness heights upstream of the first row of elements. There is a shear layer that starts over the top of the first element and increases in height as x/k increases. The reverse flow region behind the last element extends only about 1 roughness height downstream and is much weaker in strength when compared to the isolated roughness case. This may be explained by the fact that, in the isolated roughness case, the element sees a larger dynamic pressure from the flow and there is therefore a larger reverse flow region. For the distributed roughness case, however, the corresponding element on the back row of the distribution does not see as high a dynamic pressure as the isolated element due to the presence of the rows of elements ahead of it and the fact that the majority of the high energy flow has been displaced upwards by these elements; hence the corresponding reverse flow pocket is smaller and weaker.

Figure 9 shows the global flowfield variation of the mean velocity w/U_∞ for the isolated roughness and distributed roughness cases. For the isolated roughness case, at the base of the hemisphere below the location where the separation streamline strikes the hemisphere, there is a small concentrated region of negative flow due to the presence of the horseshoe vortex system. Above the point where the separation streamline hits the surface of the hemisphere there is a region of high-speed positive flow indicative of the flow accelerating upward over the

6

top of the hemisphere. Downstream of the isolated roughness there are two pockets of noteworthy flow. The dark pocket represents a region of negative flow where the separated flow is starting to head back down toward the surface of the plate due to the action of the separation vortex behind the element. The lighter pocket lower and slightly ahead of the first represents a region of upward flow also created by the separation vortex behind the element. The distributed roughness flowfield over the leading element is quite similar to the flowfield over isolated roughness element in the sense that it also has a small negative region of flow at the base of the element below the separation streamline and a region of high-speed flow over the surface of the element. Note, however, that there are no noticeable pockets of negative and positive flow downstream of the last element in the distributed roughness case. This is likely because the separated region is smaller and weaker and is not observed in the data as easily with the given contour intervals.

Figure 10 shows the global flowfield variation of the turbulence intensity u'_{rms} for the isolated roughness and distributed roughness cases. The turbulence intensity is defined in this case as the standard deviation of the velocity normalized by the freestream velocity, and it is expressed in terms of percent. It is a measure of the energy of the turbulent fluctuations of the velocity. The isolated roughness case has a concentrated region of high turbulence intensity at the base of the element where the horseshoe vortex system is located. There is also a region of high turbulence intensities just aft of the element in the shear layer that separates the outer inviscid flow from the highly viscous separated region. These high values of turbulence intensities are typical in a free shear layer across which there are large velocity gradients. Likewise, note that the general level of turbulence intensity in the wake region is significantly higher than that of the region upstream of the element. In the distributed roughness case, there is also a small region of high turbulence intensities in the horseshoe vortex region. The shear layer over the top of the elements and the region downstream of the elements exhibit high intensities indicative of high energy in the fluctuating component of the u velocity. Moreover, it is interesting to note that the turbulence intensity for the distributed roughness case is higher than the isolated roughness case downstream of the roughness in the region from about $x/k = 32$ to the end of the data at $x/k = 36$.

Figure 11 shows the global flowfield variation of the turbulence intensity w'_{rms} for the isolated roughness and distributed roughness cases. Note that the regions of higher intensities correspond with those regions of higher u'_{rms} intensities discussed above.

Local Roughness Flowfield

The following data are presented in an attempt to provide more detailed information about the flowfield immediately upstream and downstream of the isolated and distributed roughness than that available from the global flowfield. Note that the streamline plots are not true streamline plots; they are rather a representation of the flow in a 2-D plane cut out of a 3-D flowfield.

The local flowfield immediately upstream of the distributed roughness element is shown in a streamline plot, a u/U_∞ contour plot, and a w/U_∞ contour plot in Fig. 12. There are at least two primary vortices located in the recirculation region in front of the distributed roughness. Vortex 1 is closer to the element and more clearly defined than vortex 2, and the contour plots show that the velocities inside vortex 1 are higher than those of vortex 2. This indicates that vortex 1 is the stronger of the two vortices. It is interesting to also note that the streamline plot verifies the existence of a secondary vortex 1' located in between the two primary vortices. This secondary vortex was rotating in the counterclockwise direction, opposite to that of the primary vortices. The location of the two primary vortices appears to coincide with the location of the two most prominent dark bands in front of the distributed elements in the oil flow visualization shown in Fig. 7. Moreover, this streamline plot is qualitatively similar to the Jet Maze model proposed by Norman[7] and shown in Fig. 2. In Norman's model, the primary vortices are denoted by 1, 2, and 3 and the secondary vortices by 1' and 2'.

Figure 13 shows the local flowfield about the isolated roughness element in a streamline plot, a u/U_∞ contour plot, and a w/U_∞ contour plot. In the isolated roughness streamline plot, the recirculation vortices are not nearly as well defined as for the distributed roughness case. This is assumed to be a function of the location and density of LDV profiles taken in front of the isolated roughness. It is thought that a denser data set may have revealed more clearly defined vortices. It is interesting to note that the vortex in the separated region behind the element is clearly visible. The length of the separation pocket appears to be about 2 roughness heights.

Roughness Wake

Figures 14, 15, and 16 show u/U_∞ profiles for the clean case, the isolated roughness case, and the distributed roughness case at $\Delta x/k = 1$, 7, and 13.7, respectively, where Δx is the distance from the location of the profile to the trailing edge of the last roughness element.

It can clearly be seen in Fig. 14 that the reverse flow region is much larger and stronger for the isolated roughness case than for the distributed roughness case at $\Delta x/k = 1$. In fact, there is only a small region near the

wall where any reverse flow exists for the distributed case.

Figure 15 shows that at $\Delta x/k = 7$ the isolated roughness profile possesses a definite momentum deficit characteristic of a wake-type profile, while the distributed roughness profile is similar to a that of a turbulent boundary-layer profile. This description also applies to the profiles at $\Delta x/k = 13.7$ in Fig. 16 except that both the isolated and distributed profiles are more fully developed at the location further downstream. These figures seem to indicate that the flow is transitional for both the isolated and the distributed cases. The distributed case, however, is clearly more developed and closer to a fully developed turbulent profile than the isolated roughness case at all locations. This is likely because transition may be starting over the top of the distributed roughness in the shear layer. Since the first row of the distributed roughness is further upstream than the isolated roughness element, the distributed roughness presents a disturbance at an earlier point in the global flowfield than the corresponding isolated roughness case. Note that more careful analysis of the data (such as that performed by Kerho[4]) is required to determine at what point in the transition process these profiles are located.

SUMMARY

An experimental investigation of the local flowfield about large isolated and distributed roughness placed in a laminar flat-plate boundary layer has been performed. Large roughness in this sense refers to roughness with a height to boundary-layer thickness greater than unity, $k/\delta > 1$. This type of roughness is typical of the type of roughness that occurs during the initial accretion of ice on an aircraft in flight. The roughness elements were hemispherical in shape, and the test conditions were run for a nominal roughness Reynolds number (Re_k) of 3900, and k/δ varied from 2.6 to 3.5. Fluorescent oil surface flow visualization was performed for both the isolated and distributed roughness flowfields. A 2D laser-Doppler velocimeter (LDV) was used to obtain the streamwise and normal velocity profiles for the clean flowfield, the isolated roughness flowfield, and the distributed roughness flowfield. Data for the three cases were compared and analyzed. The qualitative flow visualization data was interpreted and related to the quantitative LDV data.

Results showed at least 3 identifiable primary vortices in the horseshoe vortex system upstream of the isolated roughness and at least 2 primary vortices upstream of the distributed roughness. It was shown that the recirculation region behind the isolated roughness was larger and stronger than the recirculation region behind the distributed roughness. Comparison of velocity profiles downstream of the roughness indicated

that the distributed roughness flowfield was further along in the transition process than the isolated roughness flowfield at any given location. The surface oil flow visualization produced results which compared well with the LDV data and previous research[6,7].

It may be that the increased heat transfer that is present over the smooth-rough boundary in the developing ice accretions is due, at least in part, to the local flowfield created by the vortex system that is present in front of the distributed roughness. The action of the vortices and their increased turbulence intensities would clearly enhance the local heat transfer.

The goal of the current research was to obtain a better understanding of the local flowfield around isolated and distributed roughness typical of the roughness found in initial ice accretions. It is hoped that with a better understanding of this flowfield it will be possible to improve the current ice accretion prediction capabilities. The data presented in this paper were a small subset of the entire data set taken in the experiment. Other data were taken in three separate yz planes downstream of both the isolated and distributed roughness. On and off axis data were taken so that the time-averaged 3D velocities may be calculated in each yz plane. The extended dataset will appear in future publications. It is hoped that this enhanced dataset may be used by other researchers to support the development of a new computational model to account for the effects of large roughness on the aerodynamics and heat transfer on an airfoil.

ACKNOWLEDGMENTS

REFERENCES

[1] Potapczuk, M. G., and Reinmann, J. J., "Icing Simulation: A Survey of Computer Models and Experimental Facilities," NASA TM 104366.

[2] Hansman, R. J., Yamaguchi, K., Berkowitz, B., and Potapczuk, M., "Modeling of Surface Roughness Effects on Glaze Ice Accretion," AIAA paper no. AIAA-89-0734, 27th Aerospace Sciences Meeting, January 9-12, 1989, Reno, NV.

[3] Hansman, J. R., "Microphysical Factors Which Influence Ice Accretion," Proceedings of the First

Bombardier International Workshop on Aircraft Icing/Boundary-Layer Stability and Transition, Edited by L. Paraschivoiu, Ecole Polytechnique, Montreal, Quebec, Canada, Sept. 20-21,1993.

[4] Kerho, M. F., "Effect of Large Distributed Roughness Near an Airfoil Leading Edge on Boundary-layer Development and Transition," Ph.D. Dissertation, University of Illinois at Urbana-Champaign, 1995.

[5] Shin, J., "Characteristics of Surface Roughness Associated with Leading Edge Ice Accretion," AIAA 940799, paper presented at the 32nd Aerospace Sciences Meeting, Reno, Nevada, January 10-13, 1994.

[6] Gregory, N., and Walker, W. S., "The Effects of Transition of Isolated Surface Excrescences in the Boundary Layer," British ARC, Res. Memo. 2779, 1956.

[7] Norman, R. S., "On Obstacle Generated Secondary Flows in Laminar Boundary-layers and Transition to Turbulence," Ph.D. Thesis, Illinois Institute of Technology, 1972.

[8] Acarlar, M. S., and Smith, C. R., "A study of hairpin vortices in a laminar boundary layer," *Journal of Fluid Mechanics*, vol. 175, pp. 1-41, 1987.

[9] Kendal, J. M., "Study of the effect of free-stream turbulence upon disturbances in the pre-transitional laminar boundary layer (Part I); Laminar boundary layer distortion by surface roughness; effect upon stability (Part II)," AFWAL-TR-82-3002.

[10] Corke, T. C., Bar-Sever, A., and Morkovin, M. V., "Experiments on transition enhancement by distributed roughness," Physics of Fluids, Vol. 29, pp. 3199-3213, October, 1986.

[11] Tadjfar, M., Reshotko, E., Dybbs, A., and Edwards, R. V., "Velocity measurements within boundary layer roughness using index matching," ASME Fluids Engineering Division, Vol. 33, pp. 59-73, presented at the International Symposium on Laser Anemometry, at The winter annual meeting of the American society of mechanical engineers, Miami Beach, Florida, Nov. 17-22, 1985.

[12] Khodadoust, A., "An Experimental Study of the Flowfield on a Semispan Rectangular Wing with a Simulated Glaze Ice Accretion," Ph.D. Dissertation, University of Illinois at Urbana-Champaign, 1993.

[13] TSI, Inc., *TSI Model 9306 6-Jet Atomizer Manual*, St. Paul, MN, June 1987.

[14] Coleman, H. W., and Steele, W. G., *Experimentation and Uncertainty Analysis for Engineers*, Wiley, New York, 1989.
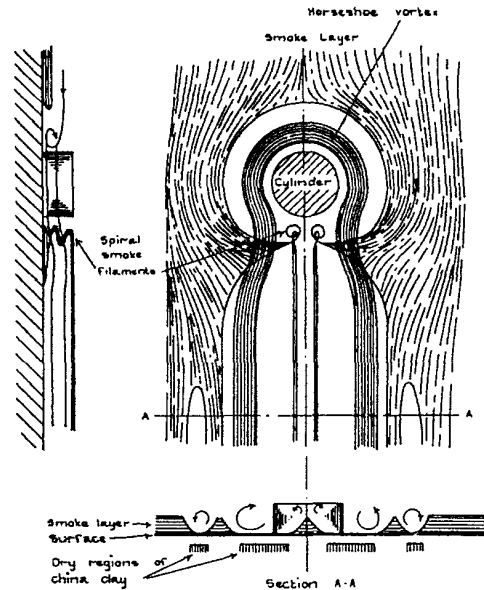
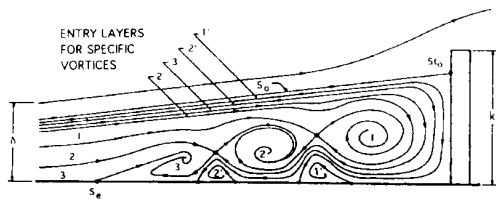Figure 1. Flowfield diagram of a cylindrical roughness element in a laminar boundary layer. Taken from Gregory and Walker[6].

Figure 2. Jet Maze model proposed by Norman[7] to describe the upstream horseshoe vortex system.
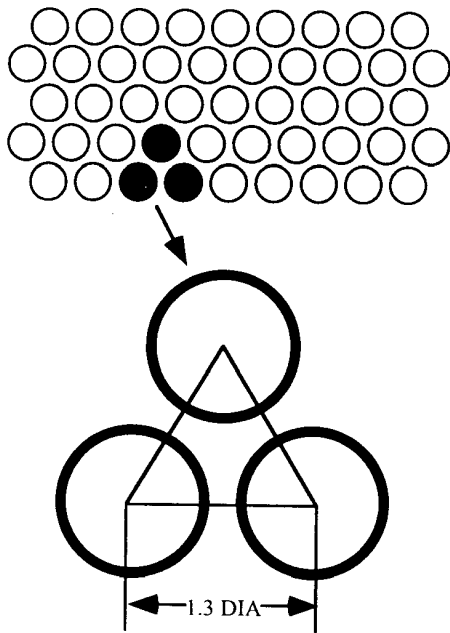
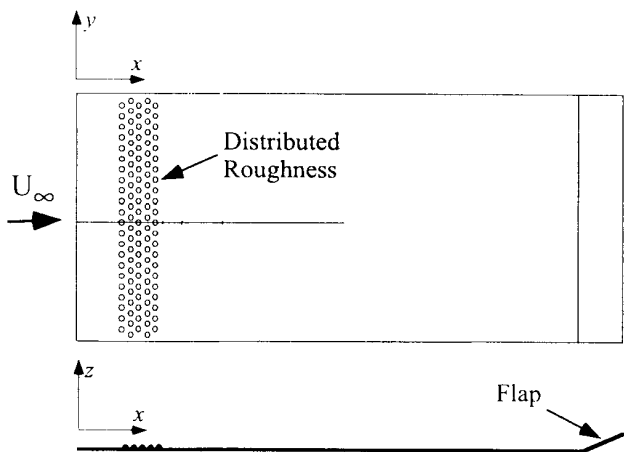

Figure 3. Distributed roughness pattern used in this study.

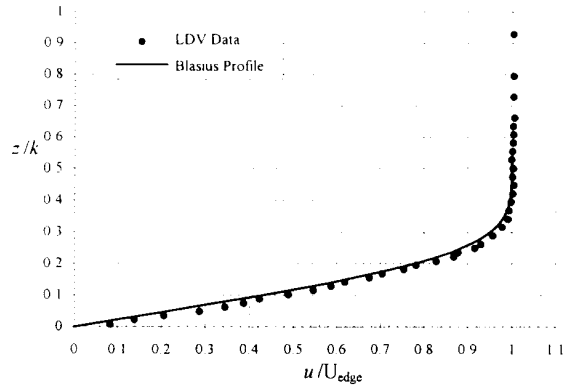Figure 4. Diagram of flat plate model used in this study.

Figure 5. Comparison of clean u/U_∞ LDV data to the theoretical Blasius solution. Note that the coordinates were normalized by the roughness height, k, to keep these profiles consistent with other data in this paper. There was no roughness present in this particular measurement.
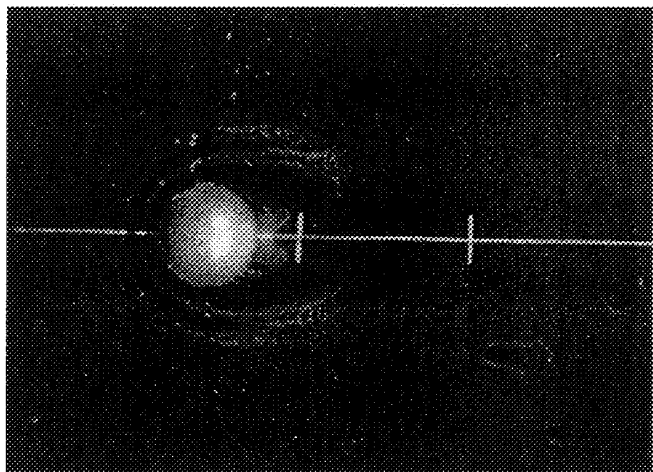

Figure 6. Fluorescent oil flow visualization of the isolated roughness flowfield.
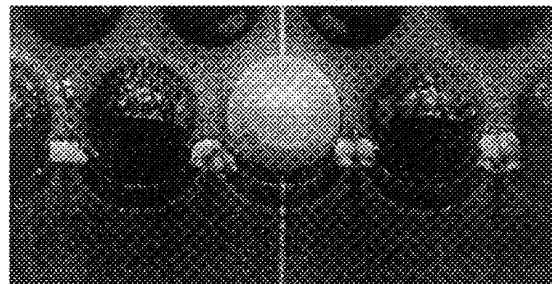
Figure 7. Fluorescent oil flow visualization of the distributed roughness flowfield.

10
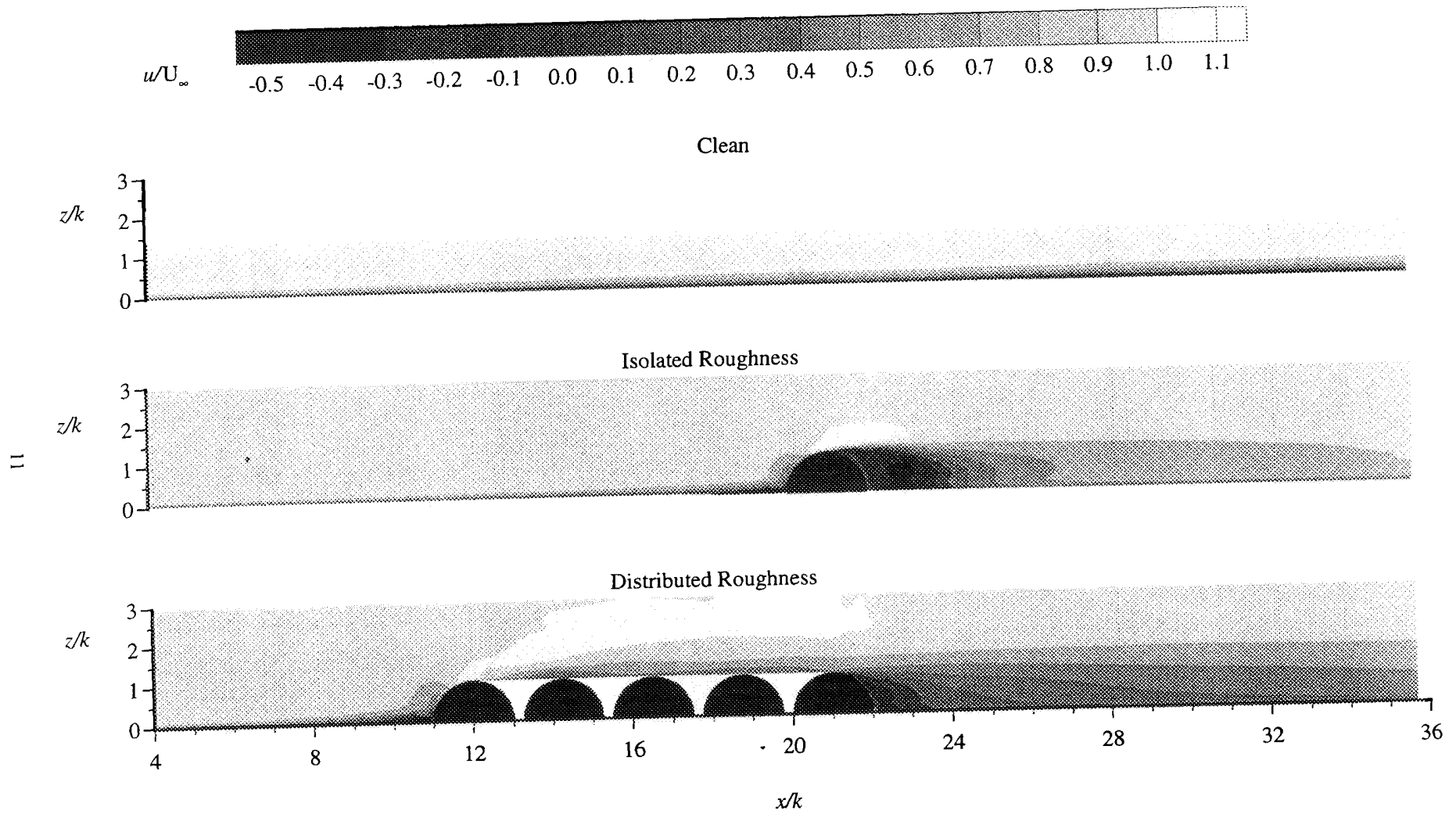
Figure 8. Contours of the mean velocity u/U_∞ for the global flowfield.
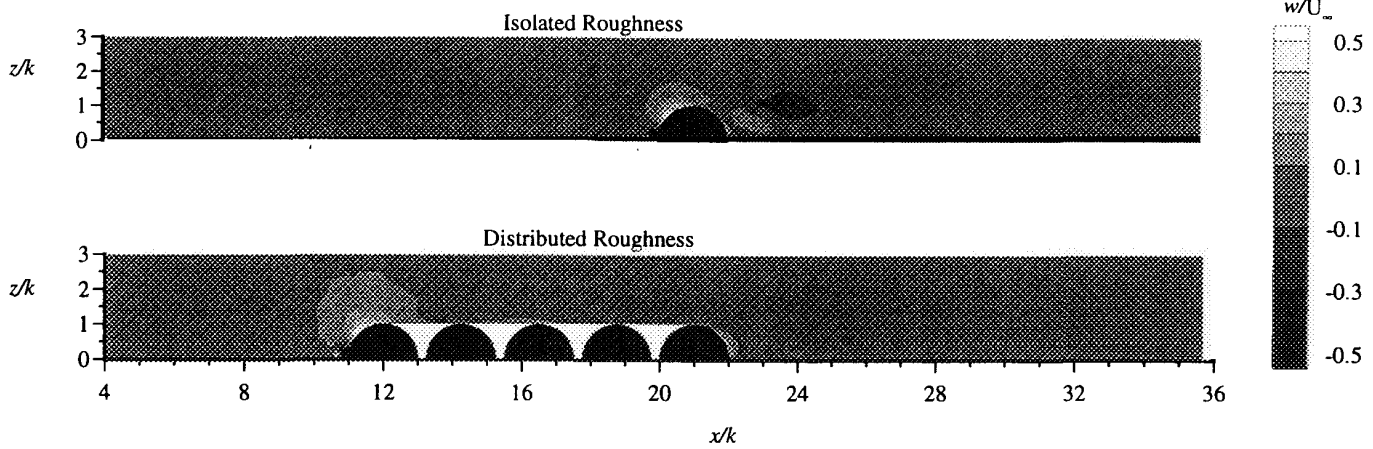
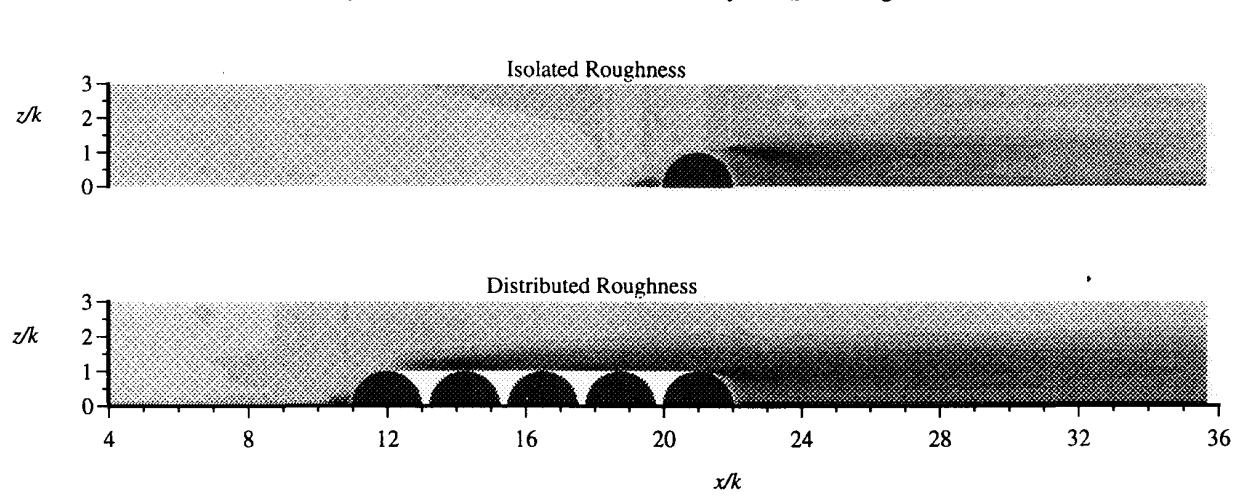Figure 9. Contours of the mean velocity w/U_∞ for the global flowfield.

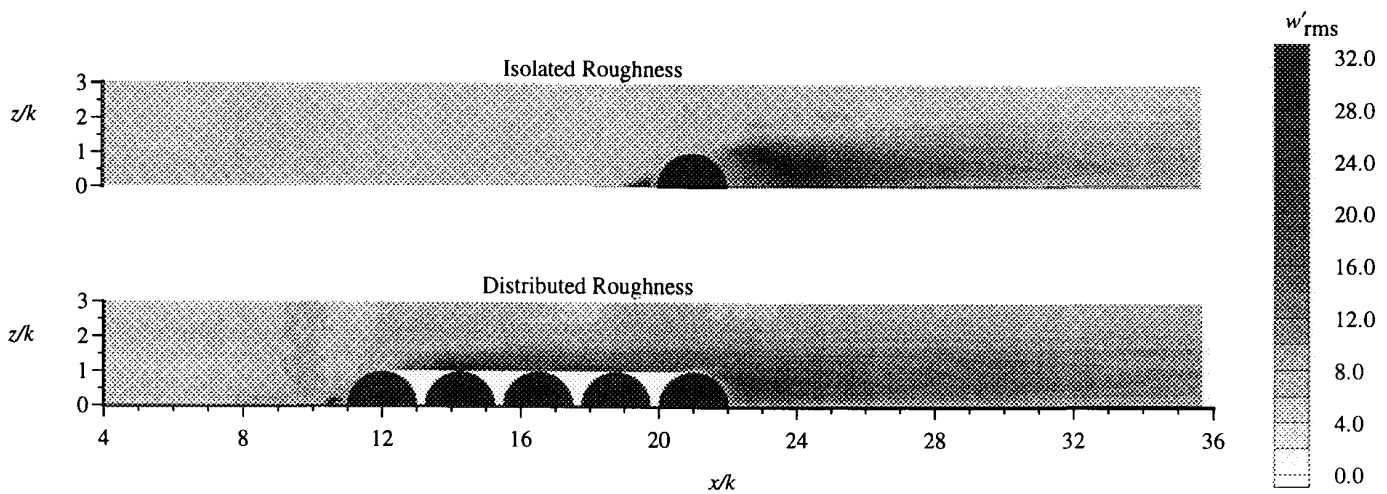Figure 10. Contours of the turbulence intensity u'_{rms} for the global flowfield.

Figure 11. Contours of the turbulence intensity w'_{rms} for the global flowfield
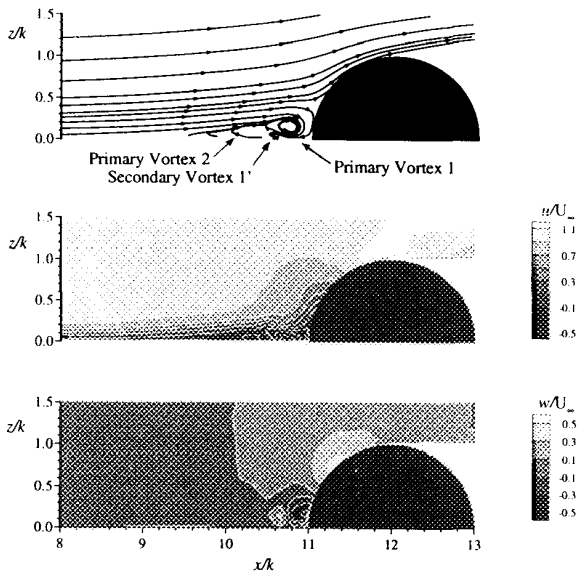
12

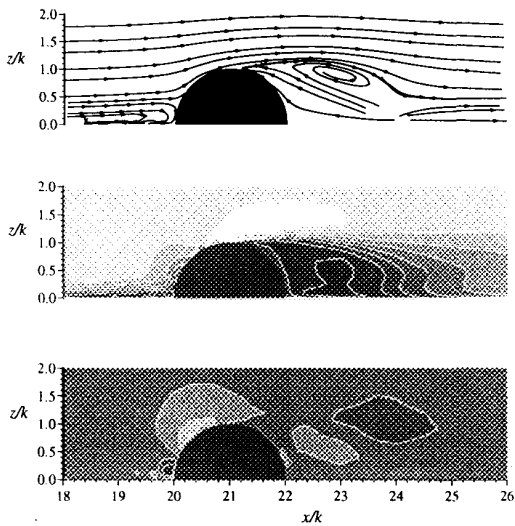Figure 12. Local flowfield upstream of the distributed roughness.

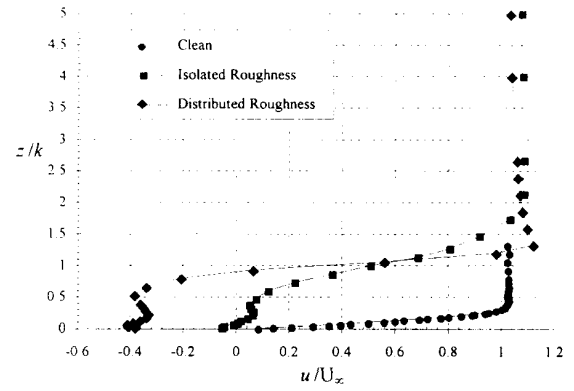Figure 13. Local flowfield about the isolated roughness element.

Figure 14. Clean, isolated roughness, and distributed roughness profiles of u/U_∞ at $\Delta x/k$=1.
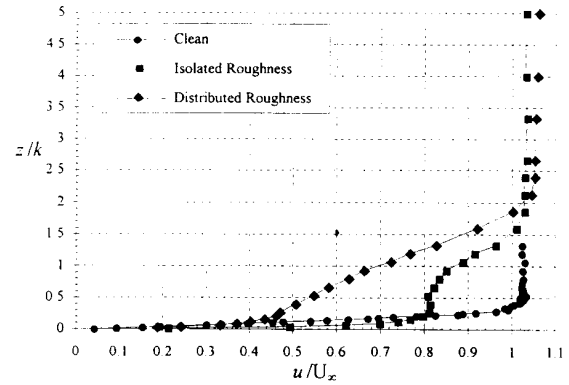

Figure 15. Clean, isolated roughness, and distributed roughness profiles of u/U_∞ at $\Delta x/k$=7.
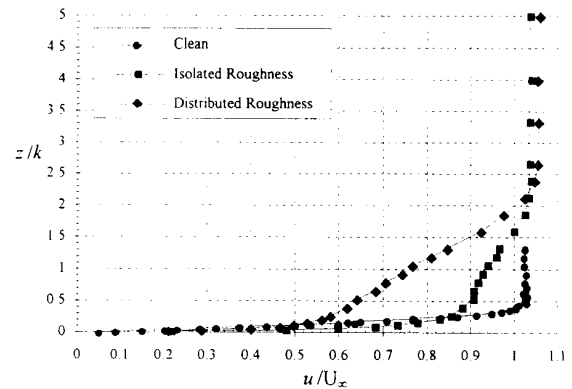

Figure 16. Clean, isolated roughness, and distributed roughness profiles of u/U_∞ at $\Delta x/k$=13.7.

13

Fig. 6

Fig. 7

Fig. 8

Fig. 9

Isolated Roughness

Distributed Roughness

w/U_∞

0.5
0.3
0.1
-0.1
-0.3
-0.5

x/k

Fig. 10

Isolated Roughness

Distributed Roughness

Fig. 11

Isolated Roughness

Distributed Roughness

Fig. 12

Primary Vortex 2
Secondary Vortex 1'
Primary Vortex 1

Fig. 13